ORIGINAL RESEARCH

Hepatic Steatosis Accompanies Pulmonary Alveolar Proteinosis

Alan N. Hunt[1], Anagha Malur[2], Tual Monfort[3], Pavlos Lagoudakis[4], Sumeet Mahajan[3], Anthony D. Postle[1], and Mary Jane Thomassen[2]

[1]Clinical and Experimental Sciences, Faculty of Medicine, [3]Institute for Life Sciences, and [4]School of Physics and Astronomy, University of Southampton, Southampton, United Kingdom; and [2]Division of Pulmonary, Critical Care and Sleep Medicine, Brody School of Medicine, East Carolina University, Greenville, North Carolina

ORCID IDs: 0000-0001-5938-2152 (A.N.H.); 0000-0002-3557-5299 (P.L.); 0000-0001-8923-6666 (S.M.); 0000-0001-7361-0756 (A.D.P.); 0000-0003-1229-7668 (M.J.T.).

Abstract

Maintenance of tissue-specific organ lipid compositions characterizes mammalian lipid homeostasis. The lungs and liver synthesize mixed phosphatidylcholine (PC) molecular species that are subsequently tailored for function. The lungs progressively enrich disaturated PC directed to lamellar body surfactant stores before secretion. The liver accumulates polyunsaturated PC directed to very-low-density lipoprotein assembly and secretion, or to triglyceride stores. In each tissue, selective PC species enrichment mechanisms lie at the heart of effective homeostasis. We tested for potential coordination between these spatially separated but possibly complementary phenomena under a major derangement of lung PC metabolism, pulmonary alveolar proteinosis (PAP), which overwhelms homeostasis and leads to excessive surfactant accumulation. Using static and dynamic lipidomics techniques, we compared (*1*) tissue PC compositions and contents, and (*2*) in lungs, the absolute rates of synthesis in both control mice and the granulocyte–macrophage colony-stimulating factor knockout model of PAP. Significant disaturated PC accumulation in bronchoalveolar lavage fluid, alveolar macrophage, and lavaged lung tissue occurred alongside increased PC synthesis, consistent with reported defects in alveolar macrophage surfactant turnover. However, microscopy using oil red O staining, coherent anti-Stokes Raman scattering, second harmonic generation, and transmission electron microscopy also revealed neutral-lipid droplet accumulations in alveolar lipofibroblasts of granular macrophage colony-stimulating factor knockout animals, suggesting that lipid homeostasis deficits extend beyond alveolar macrophages. PAP plasma PC composition was significantly polyunsaturated fatty acid enriched, but the content was unchanged and hepatic polyunsaturated fatty acid–enriched PC content increased by 50% with an accompanying micro/macrovesicular steatosis and a fibrotic damage pattern consistent with nonalcoholic fatty liver disease. These data suggest a hepatopulmonary axis of PC metabolism coordination, with wider implications for understanding and managing lipid pathologies in which compromise of one organ has unexpected consequences for another.

Keywords: pulmonary alveolar proteinosis; lipidomics; lipotoxicity; hepatic steatosis; fibrotic damage

Clinical Relevance

The demonstration of hepatic steatosis accompanying pulmonary alveolar proteinosis is a novel observation that provides further insights to the derangement of whole body lipid metabolism associated with granular macrophage colony-stimulating factor ablation. Close links between lung and hepatic lipid metabolism are established. Together they provide insights to relevant additional clinical support that may be required in pulmonary alveolar proteinosis should these experimental animal observations be recapitulated in human patients.

(Received in original form August 3, 2016; accepted in final form April 21, 2017)

This work was supported by Wellcome Trust (057405).

Author Contributions: Conception and design: A.N.H. and A.D.P.; experiments, data collection, and observations: A.N.H., A.M., T.M., and P.L.; data analysis and interpretation: A.N.H., S.M., A.D.P., and M.J.T.; drafting of the manuscript for important intellectual content: A.N.H., A.D.P., and M.J.T.

Correspondence and requests for reprints should be addressed to Alan N. Hunt, Ph.D., Clinical and Experimental Sciences, Faculty of Medicine, Room LF75, Level F, South Block, Southampton General Hospital, Tremona Road, Southampton SO16 6YD, UK. E-mail: anh@soton.ac.uk

This article has an online supplement, which is accessible from this issue's table of contents at www.atsjournals.org

Am J Respir Cell Mol Biol Vol 57, Iss 4, pp 448–458, Oct 2017

Originally Published in Press as DOI: 10.1165/rcmb.2016-0242OC on May 10, 2017
Internet address: www.atsjournals.org

Cell functions are underpinned in part by tight homeostatic control of membrane phospholipid metabolism (1). This control is regulated at the levels of synthesis, degradation, and transport, and the cumulative consequences of even very small imbalances in one or more parameters are potentially catastrophic if they are not corrected (1). To maintain equilibrium, a change in any parameter must be matched by a corresponding alteration in the others. Discordance in these mechanisms will lead to either a deficit or an excess of membrane lipid. In the former case, cell integrity and viability are compromised, and in the latter the aberrant accumulation of membrane phospholipid is often accompanied by lipotoxicity.

Lipotoxicity represents a general failure of lipid homeostasis, at the excess extreme, whereby ectopic accumulation of lipid droplets occurs in lean tissue. It is most frequently reported in the context of overfeeding or metabolic syndrome (2). Excess lipids, predominantly triacylglycerol (TAG) and cholesterol esters, accumulate in major organs, including the heart, kidney, and liver, as well as in skeletal muscle and other tissues (3). Sequelae can include cardiomyopathy (4), renal failure (5), cirrhosis (6), and sarcopenia (7). Mechanisms underlying impairments of affected cell functions include free fatty acid–mediated endoplasmic reticulum stress, ceramide formation, and oxidative damage leading to inflammation, apoptotic or necrotic cell death, and fibrosis.

Most animal models of lipotoxicity involve dietary manipulation and overfeeding. For example, excessive calorie load and obesity in rodents results in excess lipid-droplet accumulation within hepatocytes (6, 8). This has been used as a model of the pathology seen in human nonalcoholic fatty liver disease (9). Other lipotoxicities are modeled by targeted derangement and enforced imbalance of key regulatory elements of the lipid metabolism–related genome. One established human lung lipotoxic pathology is pulmonary alveolar proteinosis (PAP), characterized by an excessive accumulation of lipid-rich surfactant in the alveolar compartment (10). The most common form of PAP is autoimmune in origin (11), and antibody blocking of granulocyte–macrophage colony-stimulating factor (GM-CSF) actions is the key feature of the disease process. Construction of a murine model by genetic ablation of GM-CSF recapitulated the major elements of the human PAP phenotype, including significantly deranged lung lipid homeostasis (12, 13). Much subsequent PAP research with this model has focused on the lungs, specifically the excessive surfactant accumulation and lipotoxic overload of alveolar macrophages (AMs). AM accretion of lipid is attributed to compromised catabolic capacity (10), and affected signaling cascade(s) downstream of GM-CSF involving PPARγ have been extensively characterized (14, 15).

PAP investigations have not explored possible lipotoxic involvement in lung cell types other than AMs, or indeed more systemic consequences beyond the lung. Nevertheless, other lung pathologies show lipotoxic susceptibility in different lung cells. For example, in the lungs of obese (fa/fa) Zucker rats, ectopic lipid accumulates within the alveolar interstitium and lipofibroblasts as well as in AMs (16). Transgenic models reinforce this understanding. The targeted activation of sterol-response element-binding proteins (SREBPs) in pulmonary surfactant-producing alveolar type II (AT2) cells increases alveolar surfactant but leads to a neutral-lipid accumulation in the cells (17). By contrast, blocking SREBP action in these cells by deleting the SREBP cleavage-activating protein gene, SCAP, in lung epithelia reduces AT2 surfactant synthesis but results in a localized neutral-lipid accumulation focused on lung lipofibroblasts (18).

The possible involvement of PAP in systemic as well as local derangements of lipid homeostasis is important in the light of recent insights into AT2 cell surfactant metabolism (19). AT2 cells specialize in the synthesis, enrichment, and transient accumulation/storage (before secretion) of saturated phosphatidylcholine (PC) as the major lipid component of pulmonary surfactant (20). We previously showed that the absolute amounts of lung PC that are normally synthesized *in vivo* exceed surfactant requirements by at least an order of magnitude (19), with the excess unsaturated PC that is not destined for alveolar secretion being returned to the circulation and presumably redirected to the liver via high-density lipoproteins (HDLs). It is likely, therefore, that shifts in PAP whole-lung surfactant PC metabolism result in changes in circulatory PC flux with systemic consequences.

Here, we explored PAP PC metabolism using detailed static and dynamic lipidomic technologies (19). We coupled these technologies with lipid-focused histology to probe lung and liver responses to GM-CSF knockout (KO). We employed microscopic techniques, including oil red O (ORO) staining and transmission electron microscopy (TEM), along with more specific imaging techniques such as coherent anti-Stokes Raman scattering (CARS) for lipids and second harmonic generation (SHG) for collagen fibers. Alongside established AM lipotoxicities, we recorded significant whole-lung–tissue lipid accretion and associated fibrotic damage. We identified, for the first time, a distinctive hepatic lipotoxic phenotype including fibrotic damage, consistent with the notion that GM-CSF ablation effects extend systemically to affect aspects of whole-body lipid metabolism.

Materials and Methods

Studies were conducted in accordance with the Public Health Service Policy on Humane Care and Use of Laboratory Animals, and were approved by the East Carolina University Institutional Animal Care and Use Committee. GM-CSF KO mice have been previously described (12, 13). The animals studied were age (8–12 weeks) and sex matched to wild-type C57Bl/6 controls obtained from The Jackson Laboratory (Bar Harbor, ME). Eight or more mice per group were used except when indicated otherwise.

Mice were injected intraperitoneally with 0.1 mg D9-choline (Sigma-Aldrich, St. Louis, MO) (19) for 3 hours. After the mice were killed, the lungs were lavaged (5 × 1 ml) and bronchoalveolar lavage fluid (BALF) was collected. Cells from BALF were harvested by centrifugation and frozen, with a portion retained for differential cell counts. Lavaged lungs, livers, and plasma were snap-frozen in liquid nitrogen and stored at −80°C.

Tissues for TEM were finely diced (2-mm cubes) and collected into 4% formaldehyde, 3% glutaraldehyde in 0.1 M PIPES buffer. After 5 days and two buffer washes in 0.1 M PIPES (pH 7.2), the samples were transferred to 1% OsO_4 in 0.1 M PIPES (pH 7.2) for 1 hour, washed twice, transferred to 2% aqueous uranyl acetate for 20 minutes, and then dehydrated through successive washes in 30%, 50%,

70%, 95%, and absolute ethanol. The samples were transferred to acetonitrile for 10 minutes and then incubated overnight in acetonitrile/resin (50:50). After a final incubation in resin for 6 hours, they were embedded in fresh resin polymerized at 60°C for 24 hours.

For other microscopy methods, unfixed tissue was allowed to come to the ambient temperature of the cryostat. The tissue was mounted in OCT embedding matrix (CellPath, Newport, Powys, Wales). Sections (7 μm for ORO staining and 25 μm for CARS/SHG) were cut and placed on 3-aminopropyltriethoxysilane–coated glass slides. ORO slides were air dried, washed, and stained with ORO solution, and then counterstained with Mayer's hematoxylin. Photomicrographs were collected via a Nikon (Tokyo, Japan) microscope with a 100× oil immersion objective.

The CARS and SHG slides were air dried, PBS was added, and a coverslip was placed on top and sealed with nail varnish. Images were acquired with an in-house-built CARS- and SHG-capable, multiphoton microscope setup (21). For SHG, the 835-nm pump beam served as the excitation. Up to 30 mW of average power from both the pump and the Stokes source was delivered to the sample with no photodamage. Samples were imaged with identical laser intensity. SHG and CARS signals, passed through suitable dichroics and narrow bandpass filters, were detected in the backward direction using a nondescanned geometry with photomultiplier tube detectors simultaneously in two separate channels. SHG signals were collected using a bandpass filter at 420 (± 10) nm. Image collection was performed using ScanImage3.6 (Janelia Farms, Ashburn, VA). Image processing and analysis were performed using ImageJ (22).

Lipidomic analyses, including calculations of the absolute rates of lung-tissue PC synthesis, were undertaken as previously described (19, 23, 24).

Unpaired *t* tests were used for statistical analyses. Values were routinely expressed as the mean ± standard error of the mean (SEM), with *P* values for significance as indicated for each experiment.

Results

Lung-Compartment PC Contents and Molecular-Species Compositions

In agreement with previous observations (13, 14), GM-CSF ablation increased the PC recovered from the BALF supernatant after cell removal (by 7.5-fold; $P = 0.0024$) compared with controls (Figure 1). Unsurprisingly, the PC molecular-species composition profiles were particularly enriched in disaturated species, predominantly PC16:0/16:0 (Figure 2A), which is characteristic of surfactant.

After careful washing to remove pelleted surfactant, the PC content of cells recovered from the BALF of these affected animals, predominantly lipid-engorged macrophages, was elevated (~ 25-fold, $P < 0.0001$) compared with controls (Figure 1). This vast excess of intracellular PC in BALF cells was also characterized by specific enrichments of disaturated PC (DSPC) and monounsaturated molecular species, which is consistent with surfactant accumulation but also reflects a significant extracellular pool of surfactant that could not be removed by washing (Figure 2B). Other, characteristically cell-membrane–related PC species were much diminished in proportional representation.

The PC content of extensively lavaged lung tissue was also elevated 2.79-fold ($P = 0.024$; Figure 1), indicating significant intracellular PC retention. Mass spectrometry analysis of lipid extracts of postlavage lungs from GM-CSF–ablated animals revealed that this residual lung PC pool was also proportionally enriched in DSPC (Figure 2C), implying a steady-state increase in surfactant PC retention/storage. This was considered most likely to be in the form of more lamellar body (LB) storage, although some contribution in KO animals from extracellular surfactant resistant to the extensive lavage protocol could not be excluded.

Additional data (Figure E1 in the online supplement) showed that lavaged lung tissue phosphatidylethanolamine (PE) was unaltered in GM-CSF KO animals with regard to both content and composition. There was some significant variation in the proportions of phosphatidylinositol (PI) molecular species, with significantly more PI16:0/22:6 PI in the PAP animals. Phosphatidylglycerol and phosphatidylserine compositions were unaltered (data not shown), but no quantitation was undertaken for these phospholipids or PI.

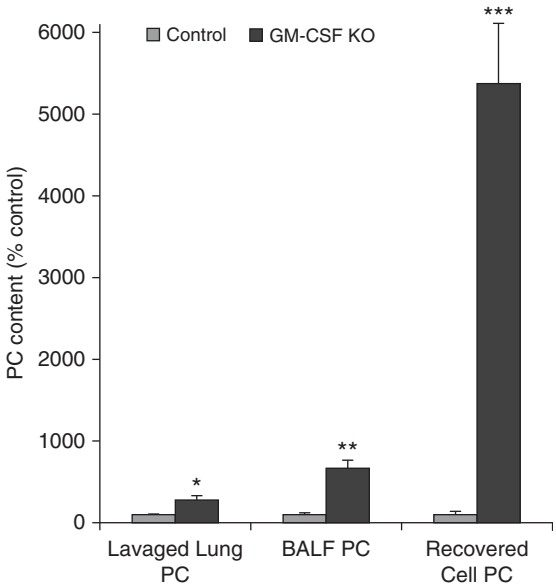

Figure 1. Phosphatidylcholine (PC) accumulations in lung compartments. The mean PC content of control samples were defined as 100% ± SEM while increased content of equivalent samples from granulocyte–macrophage colony-stimulating factor–ablated animals expressed as a percentage of relevant control mean ± SEM. Lavaged lung, $n = 12$ and 24; bronchoalveolar lavage fluid (BALF), $n = 9$ and 19; recovered cells, $n = 11$ and 14. $^{*}P < 0.02$, $^{**}P < 0.0003$, $^{***}P < 0.000002$. GM-CSF, granulocyte–macrophage colony-stimulating factor knockout; KO, knockout.

Lung PC Synthesis and Alveolar Secretion

We previously established that the normal absolute rate of mouse lung PC synthesis *in vivo* far exceeds that required for surfactant secretion alone (19), and that the

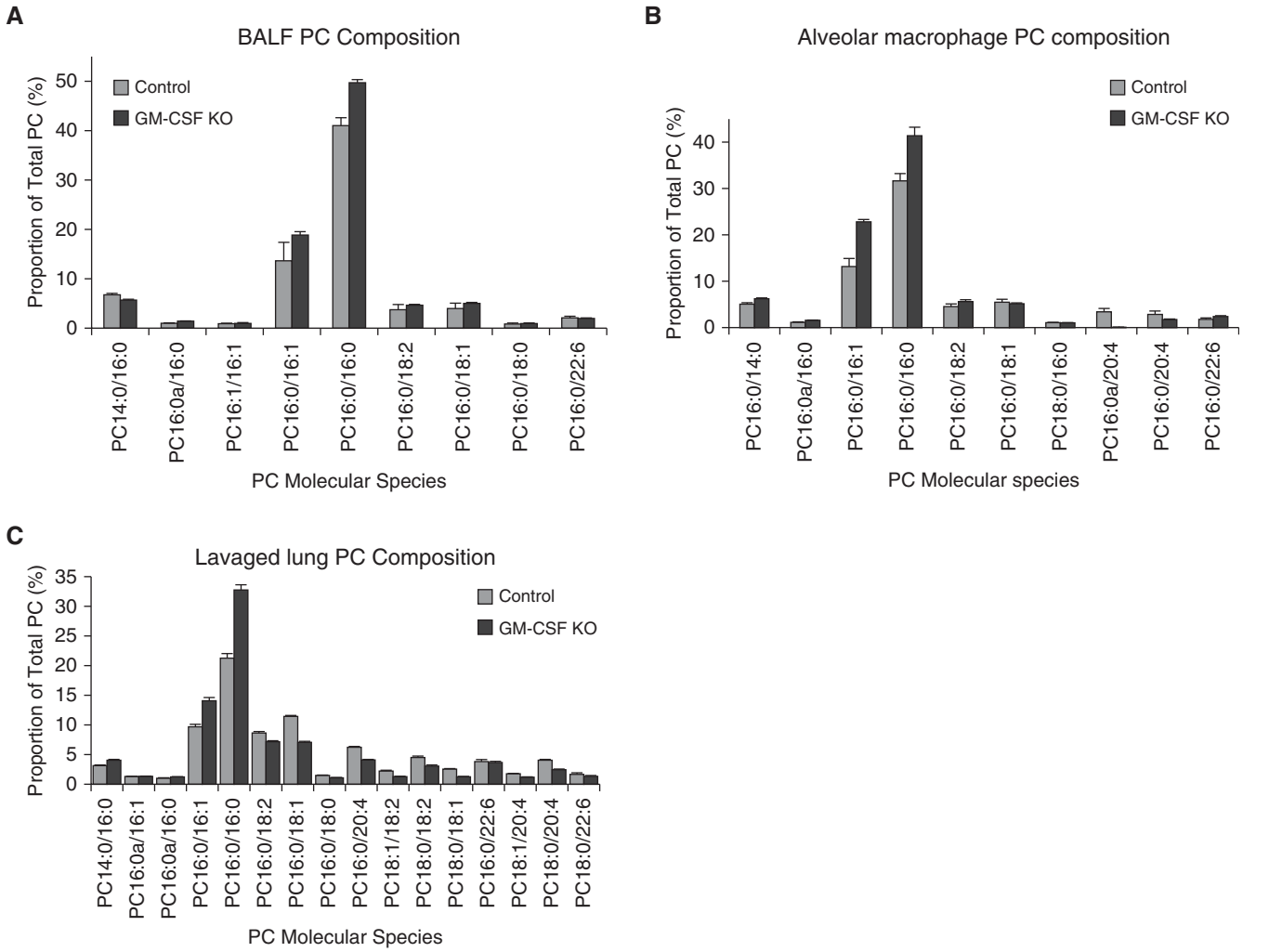

Figure 2. PC molecular species compositions in lung compartments. (*A*) Proportional representation of all PC species > 0.5% total PC in lavaged lung tissue from control and GM-CSF KO animals (mean ± SEM, n = 12 and 24). (*B*) Proportional representation of all PC species > 0.5% total PC in BALF from control and GM-CSF KO animals (mean ± SEM, n = 9 and 19). (*C*) Proportional representation of all PC species > 0.5% total PC in cells recovered from control and GM-CSF BALF (mean ± SEM, n = 11 and 14). The reported molecular species represent the experimentally ascertained dominant molecular species from the potential isobaric options.

excess PC is likely subject to the basolateral route of removal (25). Here, using a similar D_9-choline labeling protocol, we determined the absolute PC synthesis rate in control lungs over a period of 3 hours *in vivo* to be 1.582 ± 0.511 μmoles PC/g wet weight lavaged lung. In GM-CSF–ablated animals, this was significantly higher at 4.235 ± 1.444 μmoles PC/g wet weight lavaged lung (mean ± SEM, n = 4 and 12, respectively; P = 0.0037).

The calculated rate of deuterated surfactant PC secretion into the BALF of control animals at 3 hours was more than an order of magnitude lower than the synthesis rate, consistent with previous work (19), but an equivalent calculation for GM-CSF KO animals was unreliable. Deuterated DSPC was present at low levels in the BALF, indicating secretion of newly synthesized surfactant at 3 hours. However, due to a much greater dilution of the stable isotope with the excess unlabeled BALF PC, and consequent sensitivity limitations, no further meaningful inference was possible. We could not assess whether secretion rates were altered in the GM-CSF KO animals.

Plasma

Plasma lipid composition was evaluated. However, the steady-state total plasma PC contents were essentially identical between the GM-CSF KO and control animals (data not shown). The proportions of PC16:0/22:6 and PC18:0/22:6 were both significantly elevated ($P < 0.02$) in GM-CSF KO animals (Figure E2). Neutral-lipid analyses evaluating circulating cholesterol ester, diacylglycerol and TAG profiles, and content variations did not reveal any differences between groups (data not shown). Analyses of the deuterated plasma PC profiles were uninformative after 3 hours of labeling with D9-choline, because this is not an optimal time point for undertaking such analyses. Although it is possible that greater variations in the lipid profile distribution between different lipoprotein particles exist, and that some variations in absolute flux through specific

lipoprotein vectors, including HDLs, could occur, we could not address these possibilities on the basis of our data.

Livers

The 50% increase in the liver tissue PC content of GM-CSF–ablated animals from 8.31 ± 0.86 μmoles/g wet weight in controls to 12.50 ± 0.62 μmoles/g wet weight (mean ± SEM, n = 9 and 20; P = 0.001) was an unexpected and novel finding. The unsaturated nature of normal liver PC composition is well established (24), based on PC synthesized via N-methylation of liver phosphatidylethanolamine, which supports the hepatic synthesis of very-low-density lipoprotein (VLDL) (26). In control animals, as anticipated, we found that the liver tissue PC molecular-species composition was already a mostly unsaturated lipid pool, consistent with previous work (24, 26). The accumulated PC content that accompanies GM-CSF ablation resulted in a fractional superenrichment of PC16:0/18:2, PC16:0/22:6, and PC18:0/22:6, with an apparent decrease in saturated and monounsaturated molecular species (Figure 3A). However, when the same species are presented in terms of content (Figure 3B), it is strikingly clear that the saturated and monounsaturated species are actually statistically unchanged in abundance, and that polyunsaturated fatty acid (PUFA)-containing PC species are solely responsible for the additional PC mass present in GM-CSF livers.

Figure E3 shows that the elevated liver PE content and superenrichment of PUFA species are consistent with a larger pool availability for the PE N-methylation route of hepatic PC synthesis.

Lipid-Focused Tissue Histology

Having identified PC accumulations in both lung and liver tissues of GM-CSF KO mice, we investigated the spatial distribution of lipids within those tissues. We probed for potential lipotoxic pathology using (*1*) ORO staining to identify accumulation of neutral-lipid droplets, (*2*) CARS microscopy to obtain a semiquantitative spatial characterization of lipid droplets, (*3*) SHG to identify any collagen associated with fibrotic changes, and (*4*) TEM to obtain a detailed intracellular view of lipid droplet distribution.

ORO Staining of Neutral Lipid

ORO staining of lavaged lung sections (Figures 4A and 4B), which does not routinely stain surfactant-containing LBs due to their lack of neutral-lipid content, identified sporadic neutral-lipid–rich droplets in control lungs (Figure 4A). These were likely associated with lipofibroblasts (19) and there was no evidence of widespread neutral-lipid accumulation in either alveolar type I (AT1) or AT2 epithelial cells. In contrast, substantial lipid droplet accumulations in epithelial cells from the GM-CSF KO animals were evident (Figure 4B), although clearly identifying whether this affected AT1/AT2 or lipofibroblast cells, or both, required TEM (see below).

Similar staining of liver sections showed a characteristic pattern for normal mouse liver (Figure 4C), as the vast bulk of similarly sized neutral-lipid droplets was seen in the extracellular spaces, likely representing VLDL newly secreted from hepatocytes destined for the circulation. Comparable patterns of ORO staining in wild-type mouse liver have been reported previously (8). After GM-CSF ablation, however, the liver neutral-lipid content was much more heavily stained with ORO (Figure 4D), with significant intracellular deposition and with a clear steatosis that exhibited appearance characteristics of both microvesicular steatosis and the more common macrovesicular steatosis (8).

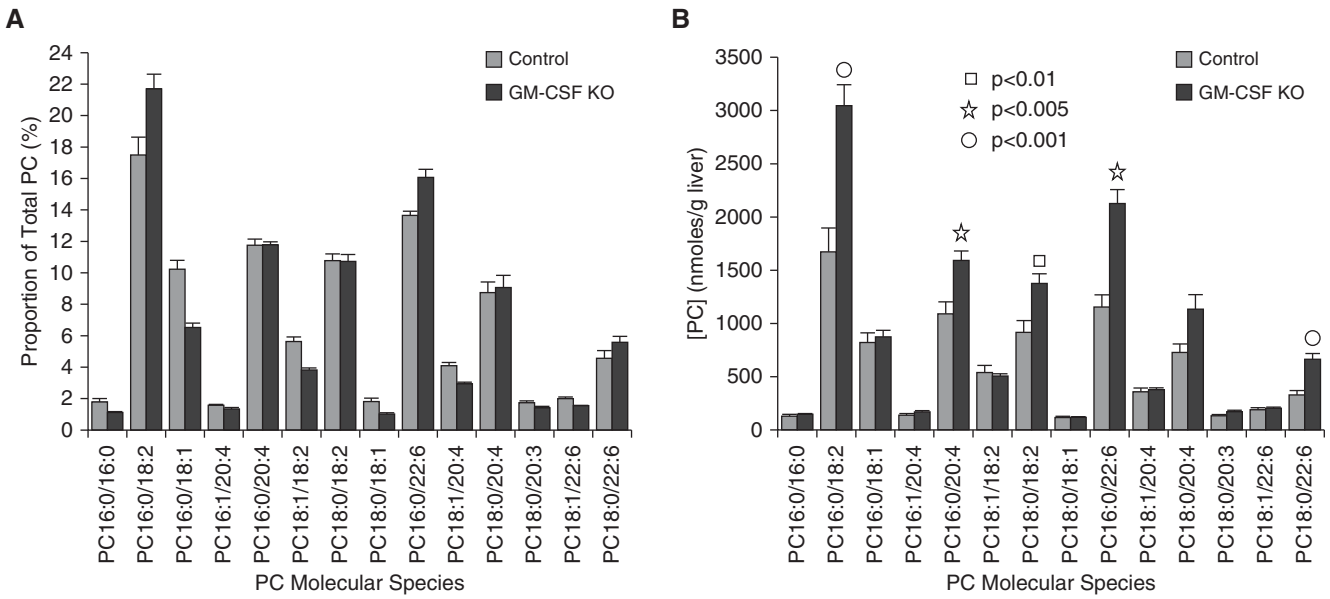

Figure 3. PC molecular species compositions and contents in whole liver. (*A*) Proportional representation of all PC species > 0.5% total PC in whole liver from control and GM-CSF KO animals (mean ± SEM, n = 8 and 20) consistent with relative enrichment of polyunsaturated PC. (*B*) Contents of the same molecular species per gram wet weight liver. With the exception of PC16:0/18:2, all PC species that were elevated significantly in GM-CSF livers as shown were polyunsaturated.

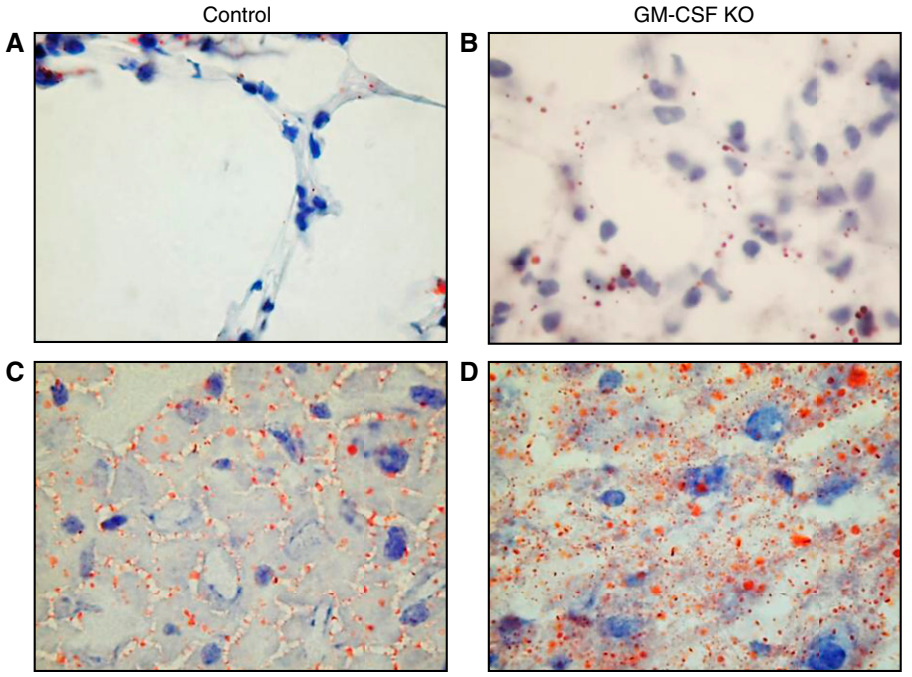

Figure 4. Oil red O (ORO) staining of lavaged lung sections and liver sections. Lavaged lung and liver samples were stained with ORO, counterstained with Mayer's hematoxylin, and observed using a ×100 oil immersion lens. (*A*) Representative control lavaged lung section with sporadic ORO-stained inclusions. (*B*) Representative GM-CSF lavaged lung with many more ORO-stained inclusions, apparently in alveolar type 1 (AT1) respiratory epithelia. (*C*) Representative control liver section with ORO-stained droplets distributed largely in the sinusoids. (*D*) Representative GM-CSF liver section with widespread ORO-stained lipid droplet inclusions of varying size within hepatocytes as well as sinusoids, a pattern consistent with steatosis.

CARS Microscopy

CARS microscopy is an imaging technique that is increasingly being utilized in biomedical applications (27). It has been widely applied to image lipids and their structures in cells and tissues. It provides a noninvasive, nondestructive, and label-free modality to selectively image lipids in intact cells and tissue without the use of complex procedures for sample preparation and histopathological examination. Examples of its use include the differential diagnosis of lung carcinoma (28) and quantification of hepatic lipid in liver tissue (8). In the liver, it has been shown that CARS can be used to evaluate hepatic microvesicular steatosis by detecting lipid droplets and quantifying their number and size (29). Moreover, CARS signal intensities from lipid droplets are consistent with their neutral-lipid content, and CARS microscopy is more sensitive than ORO analyses.

Using CARS, we examined lavaged lung tissue and corresponding liver tissue sections from control and GM-CSF KO animals. The images presented in Figures 5 and 6 show an increased amount of lipid droplets in both cases of tissue from GM-CSF KO mice compared with controls, as quantified in Table 1. Lavaged lung shows a huge increase in the GM-CSF KO signal compared with controls (Table 1). The increase in lipid content is equally profound for liver from GM-CSF KO mice compared with controls (Table 1). Although the overall increase in lipid droplets is clear, a change in size distribution is also observed. In both lung and liver tissues, there is an increase in the relative number of medium and large lipid droplets compared with small lipid droplets.

SHG Microscopy

SHG imaging is well established for imaging collagen fibrillar structures in cells and tissues (30). In this work, SHG imaging was performed simultaneously with CARS microscopy. Thus, signals from the same areas were routinely acquired (Table E1). Unexpectedly, the collagen amount and distribution increased significantly in both GM-CSF KO lung and liver, consistent with fibrotic damage accompanying lipid accumulation in both tissues. Liver fibrosis was confirmed histologically in GM-CSF KO animals by use of Sirius Red staining (Figure E4), which showed both hepatic terminal venule fibrosis and a more diffuse collagen fiber deposition throughout the tissue. Lavaged lung slices could not be efficiently retained on the slides during staining and thus were not amenable to histology.

TEM

TEM of lung sections (Figures 7A and 7B) confirmed observations from ORO staining and CARS imaging, but also provided information about the spatial distribution of lipids at the individual cell level. Because lavaged lung tissue did not respond well to TEM fixation, unlavaged lungs were used. In normal, unlavaged lungs (Figure 7A) there was no evidence of lipid droplet accumulation alongside LBs in AT2 cells or in AT1 epithelia or lipofibroblasts, whereas in unlavaged lungs from GM-CSF KO animals, lipid droplets were clearly confined to lipofibroblast cells, with no obvious AT2/AT1 accumulation (Figures 7B and E5). Taken together, these data identify lipofibroblast cells as the site of a major accumulation of potentially lipotoxic neutral lipid in the GM-CSF animals.

For control livers (Figure 7C), the majority of lipid material present was estimated in a size range consistent with VLDL particles previously described in mice (31). In the case of GM-CSF KO animals, the livers show at least three types of lipid particles. In addition to likely nascent VLDL-sized lipids, there are larger lipid droplets, many of which are clearly bounded by a lipid bilayer (Figures 7D and 7E). These would be consistent with macrovesicular lipid droplets. At higher magnification (Figure 7E), it is clear that there are significant "bunch of grapes–like" clusters of very small, microvesicular lipid droplets throughout the cytoplasm of hepatocytes. The accumulation of hepatic lipid in this PAP-linked steatosis is largely confined to hepatocytes, with no apparent Kupffer cell involvement.

Discussion

Homeostatic regulation in metabolic systems ensures that they can maintain

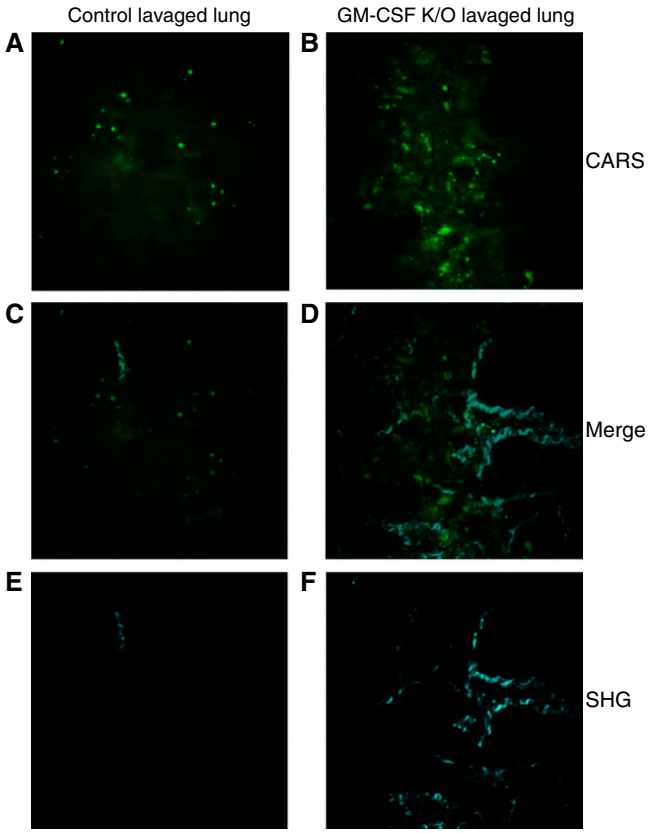

Figure 5. Coherent anti-Stokes Raman scattering (CARS) and second harmonic generation (SHG) of lung sections. Lavaged lungs from control and GM-CSF KO animals were subjected to CARS and SHG microscopy. *A* and *B* show CARS images that confirm the significant increases in lipid droplets present in GM-CSF lungs. *C* and *D* show the respective overlays of images *A* with *E*, and *B* with *F* and define the spatial relationships between lipid accretion and fibrotic changes. *E* and *F* show the SHG images of the same areas, which show a pattern of increased collagen fibers in the GM-CSF KO lungs.

equilibrium within a normal range of values when challenged by external stressors. For lipid metabolism, it is the combination of lipid uptake, synthesis, degradation/turnover, and export that is balanced to preserve cell and tissue integrity without lipid excess or deficit. Any large and sustained change in one or more of these factors has the potential to shift the equilibrium position beyond an organism's ability to compensate effectively. This is evident for the deranged surfactant metabolism that is characteristic of PAP (10). In PAP, the lung lipid metabolism steady-state position lies significantly outside of the normal range. So, as a result of defective AM function and an associated accumulation of excess lipoproteinaceous material, it is unsustainable without therapeutic intervention(s) that target the removal of alveolar surfactant congestion. Unsurprisingly, therefore, many PAP studies have addressed the respiratory sequelae stemming from a compromised or blocked capacity for alveolar gas exchange. Detailed lipidomic evaluations of pulmonary tissue PC synthesis, secretion, and turnover in PAP and any distal tissue sequelae have not been well documented.

Our lipidomic analyses of lungs and livers, and use of complementary modes of histopathology confirmed much of what was already known. In addition, we identified new phenotypic characteristics. GM-CSF ablation, in addition to producing substantial accumulations in BALF surfactant and AM accretion of lipotoxic material, is characterized by tissue lipotoxicity in both whole-lung and liver tissues. In particular, the steatoses in lipofibroblast cells and whole liver from GM-CSF KO animals are novel observations in this model, as is the pattern of associated liver fibrosis shown by SHG. Moreover, the increased flux through lung PC biosynthesis was unexpected, and in the light of previous observations (11) suggests that increased basolateral secretion of PUFA-enriched PC from the lungs likely accompanies GM-CSF ablation.

The PAP-associated, parallel accumulations in whole-lung PC and liver PC are striking, without an immediately obvious rationale for linkage. The simplest explanation is coincidence. The lung and liver both synthesize mixed-composition PC species but retain predominantly saturated and unsaturated molecular species, respectively, reflecting the distinct requirements of each tissue to maintain appropriate lipid synthesis and secretion capacity. The lung requires saturated PC for pulmonary surfactant production, whereas the liver needs unsaturated PC species for VLDL construction and secretion. The obvious explanation, however, cannot account for the observed GM-CSF KO–associated increase in liver PC or the enrichment on PUFA-containing PE species (Figure E2), which is the substrate for the PE N-methylation pathway of PC biosynthesis (32). An alternative teleology involving a highly regulated interaction between the two organs, as well as a complementary lipid exchange to ensure optimal resource and energy utilization, has not yet been explored. However, the emerging pattern of data from lipidomic studies is beginning to point to a likely coordination of mechanisms that, at least indirectly, intimately link the PC metabolism of both organs. Moreover, it suggests that significant perturbation of PC homeostasis at the level of one organ, such as that manifest in the PAP lung, may in turn have dramatic consequences for whole-body PC/lipid metabolism.

Before DSPC is secreted, the lung synthesizes, enriches, and transiently stores it as an LB surfactant (20). The absolute amounts of lung PC that are synthesized *in vivo* exceed whole-lung requirements by an order of magnitude (19), with the excess, unsaturated PC that is not destined for alveolar secretion being returned via a basolateral route (25, 33, 34) to the circulation. Indeed, the lung itself may be second only to the liver in the secretion of PUFA-rich lipoprotein into the circulation, albeit as an HDL destined for liver recycling rather than as a VLDL. Through a combination of *de novo* synthesis via the N-methylation pathway (24) and salvage from lipoprotein remnants, including HDL (32), the liver amasses PUFA-rich PC for

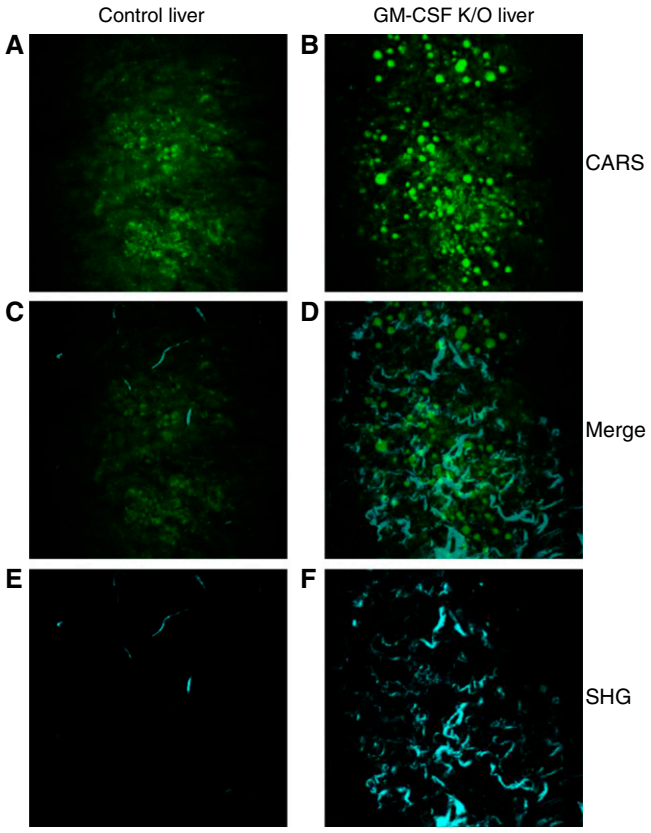

Figure 6. CARS and SHG of liver sections. Livers from control and GM-CSF KO animals were subjected to CARS and SHG microscopy. *A* and *B* show CARS images which confirm significant increases in number and size of lipid droplets present in GM-CSF livers. *C* and *D* show the respective overlays of images *A* with *E*, and *B* with *F* and define the spatial relationships between lipid accretion and hepatic fibrotic changes. *E* and *F* show the SHG images of the same areas which show a pattern of significantly increased collagen fiber depositions in the GM-CSF KO livers.

VLDL construction before the PC is distributed via the circulation (32). More saturated hepatic PC species predominantly synthesized through the cytidine diphosphocholine pathway (24) are segregated and preferentially secreted with the bile (33). Accordingly, unlike the majority of organs, the lung and liver are each responsible for the secretion or export of significant amounts of both saturated and unsaturated PC.

Given these observations, and despite previous demonstrations of anterograde (via VLDL) and retrograde (via HDL) lipid-transfer capacities that link the lung and liver, it is surprising that a potential coordination between these two organs has received little attention. Our data add weight to the possibility that these spatially segregated but apparently complementary phenomena operate in concert.

Newly synthesized lung PC does not display the same extent of saturation enrichment that is characteristic of a mature, secreted surfactant PC pool (20). Instead, progressive enrichment of saturated PC species operates to achieve the final surfactant PC composition in the alveolar space, a process referred to as remodeling. The conventional understanding of remodeling derives largely from work with cell-free homogenates (35–37) rather than from quantitative studies *in vivo*. It views the main route to saturation enrichment as a molecule-level, post-synthesis acyl exchange process to remove unsaturated fatty acids, followed by replacement with an acyl-coenzyme A–dependent saturated fatty acid (35, 36). However, our data (19) indicate that in the mouse *in vivo*, a sufficient synthesis of surfactant DSPC *de novo* is continuously maintained *in vivo* and is able to keep pace with physiological demands. There is no need *a priori* to resort to the conventional interpretation of significant acyl-chain remodeling of newly synthesized material (35, 36), provided that the newly synthesized unsaturated PC excess is quickly exported from the lung. This startling but experimentally verified observation presents a puzzle: how is that excess unsaturated PC recycled away from the lung?

Table 1. CARS Quantification

			Size (% of Total Number of Lipid Droplets)		
		CARS Image Intensity ± SD (per Image FOV)	< 1 μm² (Small)	1–5 μm² (Medium)	> 5 μm² (Large)
Lavaged lung	Control	107.7 ± 34.4	72.3	25.2	2.5
	GM-CSF KO	300.7 ± 34.2	70.7	25.2	4.1
Liver	Control	193.1 ± 49.9	80.3	18.9	0.8
	GM-CSF KO	413.5 ± 235.3	68.7	26.6	4.7

From three samples each of control and granulocyte–macrophage colony-stimulating factor knockout (GM-CSF KO) lung and liver tissues, 10 fields of view (FOV) were selected (i.e., 30 for each group) and subjected to coherent anti-Stokes Raman scattering (CARS) imaging. Upon subsequent image analyses, the distribution of lipid droplets was characterized using arbitrary size ranges broadly defined as small, medium, and large. The CARS image intensity reflects the lipid concentration, permitting semiquantitative assessment of the total lipid change. Increases in total lipid and droplet sizes are readily apparent in both the lungs and livers of GM-CSF KO animals.

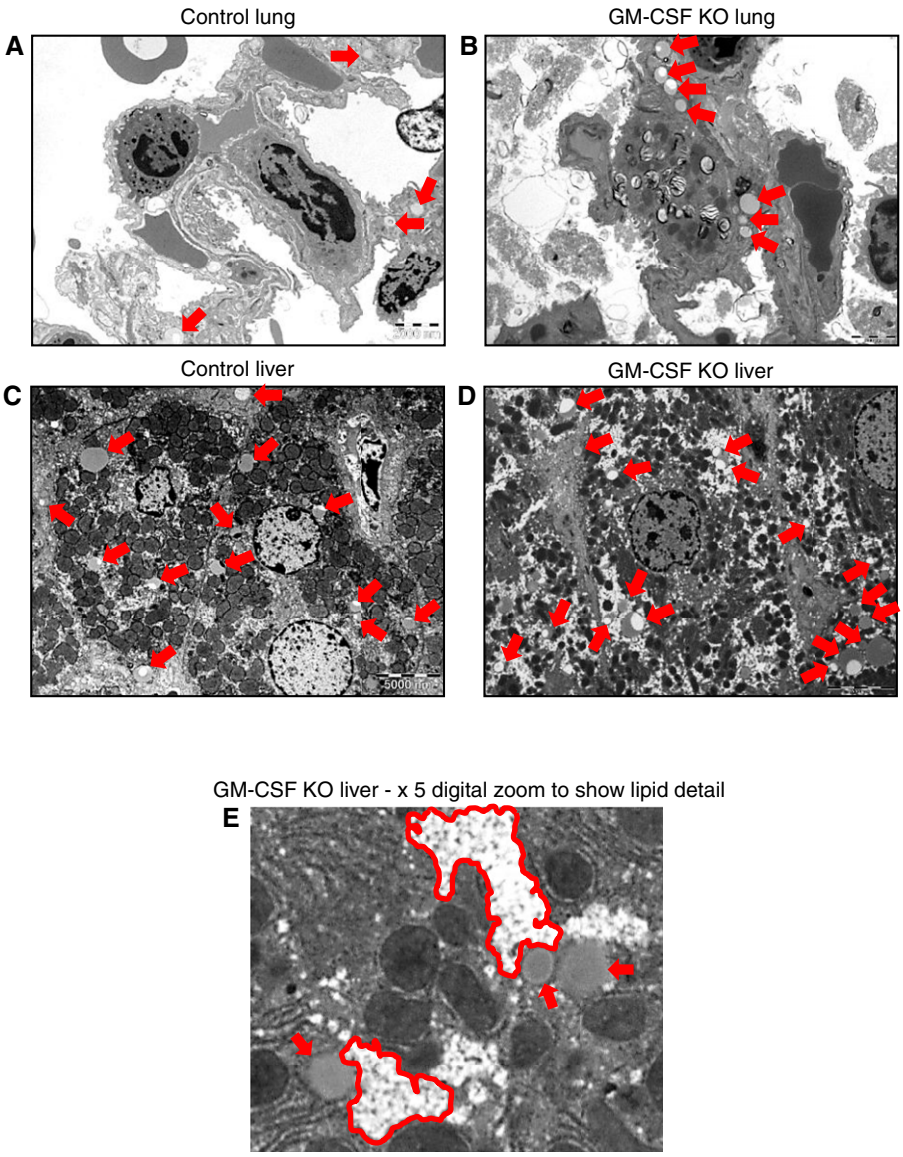

Figure 7. Transmission electron microscopy (TEM) of lung and liver tissues. Unlavaged lungs and livers from control and GM-CSF KO animals were subjected to TEM. For control lungs, 12 distinct image fields were collected and analyzed from three grids. For GM-CSF KO lungs, 17 distinct image fields were collected and analyzed from four grids. For control livers, 9 distinct image fields were collected and analyzed from 3 grids. For GM-CSF KO livers 12 distinct image fields were collected and analyzed from 4 grids. *Scale bars* are 2,000 nm and 5,000 nm for lung tissue and liver tissue, respectively. (*A*) Control lung: representative image showing a few sporadic lipid droplets (indicated by *red arrows*) but no consistent pattern. (*B*) Representative image showing accumulations of lipid droplets largely confined to lipofibroblast cells, with no indication of involvement of the adjacent AT2 or AT1 cells. A larger version of *B* is presented in Figure E5, which shows more detailed labeling of cells and lipid contents. (*C*) Control liver: representative image showing the presence of a number of lipid droplets (*red arrows*), some of which consist of nascent lipoproteins and others that are more likely lipid stores. (*D*) GM-CSF KO liver, representative image showing a much wider range of lipid droplets (*red arrows*), which in addition to lipoproteins reveal, when zoomed in upon in *E*, clusters of very small droplets (outlined in *red*) alongside larger droplets bounded by lipid bilayers.

Even under normal metabolic parameters, steady-state enrichment of surfactant DSPC in the lung requires that the significant excess of newly synthesized PUFA-enriched PC must be removed from the lung environs. PC remodeling in this excess-synthesis scenario therefore becomes a high-capacity, selective, PUFA-enriched PC species removal process rather than a high-volume breakdown and reconstruction mechanism. In addition to being more energetically efficient, this process would enable the established acyl-remodeling mechanism to correct "mistakes" and effectively tailor LB compositions for a particular purpose.

The export of PUFA-rich PC from AT2 cells involves basolateral transport to nascent HDL particles that are subsequently returned to the liver for reuptake and recycling. Retrograde transport of PC facilitates HDL construction and reverse cholesterol transport from peripheral tissues (38). The export of excess polyunsaturated PC likely accompanies cholesterol secretion via basolateral transport. Two ABC transporter proteins with recognized roles in cholesterol and phospholipid homeostasis, ABCA1 and ABCG1 (39), are expressed in both AMs and lung epithelia. Murine ABCA1 KO (33) and ABCG1 KO (40) both result in a phenotype resembling PAP, with alveolar proteinosis and lung accumulation of surfactant and neutral lipid. Moreover, functional ABCA1 and ABCG1 both appear to be required in AMs and epithelia for effective alveolar lipid management, since increases in AM ABCA1 after ABCG1 ablation do not rescue the phenotype (41). AMs from human patients with PAP also have decreased levels of ABCG1 expression and increased ABCA1, supporting that idea (41). Furthermore, studies have shown that cholesterol efflux to preformed HDL specifically requires ABCG1, whereas efflux to apoA1 requires ABCA1 (42).

The HDL returned from the lung to the liver likely arises both from lipid transfer to circulating nascent lipoprotein and via *in situ* construction *de novo* from lung-tissue–synthesized Apo-A1 (43). Capacity for *de novo* pulmonary HDL construction exists in humans and mice and operates with increases in circumstances where surfactant is known to accumulate (44) including perinatal surges in surfactant synthesis and storage where synchronous increases in lung parenchymal Apo-A1 mRNA production occur (43, 44).

The elevated unsaturated PC content observed in the liver after GM-CSF ablation suggests either a reduced rate of lipoprotein secretion resulting in a larger, unsecreted pool or an increased rate of reuptake of HDL enlarging the steady-state pool. Quantitative assessments of the hepatic uptake of HDL particles have established that 50% of the

HDL PC PUFA is directed to transient TAG storage and the other half is directly reclaimed for VLDL construction and secretion (32). Any shift in the equilibrium position that would accompany even small but sustained increases in HDL uptake outside of the normal range could mandate larger transient PC and TAG pools. Once these pools are of sufficient magnitude, steatosis may result. Our data strongly point to a mixed steatotic pattern in the liver of GM-CSF KO animals, in which both microvesicular and macrovesicular characteristics are apparent.

The fibrotic damage evidenced by the collagen fibrils present in both the lung and the liver reflects that seen elsewhere in cases of lipotoxicity (45), pointing to sustained inflammatory responses to lipid accumulation that have injurious consequences. Interestingly, this hepatic damage in PAP may have a reciprocal relationship with that seen in the lung and AM lipotoxicity reported in an alcoholic liver cirrhosis model (46). The PAP literature suggests that hepatic pathology is not commonly recognized, most likely due to minimal prior exploration of the possibility. However, reported human PAP pathology, at least in one specific genetic cohort, includes a hepatomegaly component that may stem from lipid accumulation and relate to our observations (47). Moreover, a study of bleomycin-induced fibrosis showed that liver steatosis can arise alongside the lipid metabolism changes that follow lung damage and tissue repair (48). These findings add further weight to the idea of a coordinated hepatopulmonary axis of lipid metabolism. Deranged hepatopulmonary coordination of lipid metabolism may be a common phenomenon that merits closer examination in both primary lung and liver diseases. ■

Author disclosures are available with the text of this article at www.atsjournals.org.

Acknowledgments: The authors thank Mr. Jon Ward (Histochemistry Research Unit, University of Southampton) for OCT embedding and cutting of tissues, and ORO and Sirius red staining. We also thank Dr. Anton Page (Biomedical Imaging Unit, University of Southampton) for assisting with and processing samples for TEM. The mass-spectrometry elements of this work were supported by an equipment grant from The Wellcome Trust (reference 057405).

References

1. Jackowski S. Cell cycle regulation of membrane phospholipid metabolism. *J Biol Chem* 1996;271:20219–20222.
2. Unger RH, Clark GO, Scherer PE, Orci L. Lipid homeostasis, lipotoxicity and the metabolic syndrome. *Biochim Biophys Acta* 2010;1801: 209–214.
3. Szendroedi J, Roden M. Ectopic lipids and organ function. *Curr Opin Lipidol* 2009;20:50–56.
4. Haffar T, Bérubé-Simard F, Bousette N. Impaired fatty acid oxidation as a cause for lipotoxicity in cardiomyocytes. *Biochem Biophys Res Commun* 2015;468:73–78.
5. Guebre-Egziabher F, Alix PM, Koppe L, Pelletier CC, Kalbacher E, Fouque D, Soulage CO. Ectopic lipid accumulation: A potential cause for metabolic disturbances and a contributor to the alteration of kidney function. *Biochimie* 2013;95:1971–1979.
6. Gaemers IC, Stallen JM, Kunne C, Wallner C, van Werven J, Nederveen A, Lamers WH. Lipotoxicity and steatohepatitis in an overfed mouse model for non-alcoholic fatty liver disease. *Biochim Biophys Acta* 2011;1812:447–458.
7. Turpin SM, Ryall JG, Southgate R, Darby I, Hevener AL, Febbraio MA, Kemp BE, Lynch GS, Watt MJ. Examination of 'lipotoxicity' in skeletal muscle of high-fat fed and ob/ob mice. *J Physiol* 2009;587: 1593–1605.
8. Kochan K, Maslak E, Krafft C, Kostogrys R, Chlopicki S, Baranska M. Raman spectroscopy analysis of lipid droplets content, distribution and saturation level in non-alcoholic fatty liver disease in mice. *J Biophotonics* 2015;8:597–609.
9. Mota M, Banini BA, Cazanave SC, Sanyal AJ. Molecular mechanisms of lipotoxicity and glucotoxicity in nonalcoholic fatty liver disease. *Metabolism* 2016;65:1049–1061.
10. Carey B, Trapnell BC. The molecular basis of pulmonary alveolar proteinosis. *Clin Immunol* 2010;135:223–235.
11. Trapnell BC, Carey BC, Uchida K, Suzuki T. Pulmonary alveolar proteinosis, a primary immunodeficiency of impaired GM-CSF stimulation of macrophages. *Curr Opin Immunol* 2009;21:514–521.
12. Dranoff G, Crawford AD, Sadelain M, Ream B, Rashid A, Bronson RT, Dickersin GR, Bachurski CJ, Mark EL, Whitsett JA, *et al*. Involvement of granulocyte-macrophage colony-stimulating factor in pulmonary homeostasis. *Science* 1994;264:713–716.
13. Ikegami M, Ueda T, Hull W, Whitsett JA, Mulligan RC, Dranoff G, Jobe AH. Surfactant metabolism in transgenic mice after granulocyte macrophage-colony stimulating factor ablation. *Am J Physiol* 1996; 270:L650–L658.
14. Baker AD, Malur A, Barna BP, Ghosh S, Kavuru MS, Malur AG, Thomassen MJ. Targeted PPARγ deficiency in alveolar macrophages disrupts surfactant catabolism. *J Lipid Res* 2010;51: 1325–1331.
15. Malur A, Baker AD, McCoy AJ, Wells G, Barna BP, Kavuru MS, Malur AG, Thomassen MJ. Restoration of PPARγ reverses lipid accumulation in alveolar macrophages of GM-CSF knockout mice. *Am J Physiol Lung Cell Mol Physiol* 2011;300:L73–L80.
16. Foster DJ, Ravikumar P, Bellotto DJ, Unger RH, Hsia CC. Fatty diabetic lung: altered alveolar structure and surfactant protein expression. *Am J Physiol Lung Cell Mol Physiol* 2010;298:L392–L403.
17. Plantier L, Besnard V, Xu Y, Ikegami M, Wert SE, Hunt AN, Postle AD, Whitsett JA. Activation of sterol-response element-binding proteins (SREBP) in alveolar type II cells enhances lipogenesis causing pulmonary lipotoxicity. *J Biol Chem* 2012;287:10099–10114.
18. Besnard V, Wert SE, Stahlman MT, Postle AD, Xu Y, Ikegami M, Whitsett JA. Deletion of Scap in alveolar type II cells influences lung lipid homeostasis and identifies a compensatory role for pulmonary lipofibroblasts. *J Biol Chem* 2009;284:4018–4030.
19. Postle AD, Henderson NG, Koster G, Clark HW, Hunt AN. Analysis of lung surfactant phosphatidylcholine metabolism in transgenic mice using stable isotopes. *Chem Phys Lipids* 2011;164:549–555.
20. Goss V, Hunt AN, Postle AD. Regulation of lung surfactant phospholipid synthesis and metabolism. *Biochim Biophys Acta* 2013;1831:448–458.
21. McKenzie Z, Kendall M, Mackay RM, Whitwell H, Elgy C, Ding P, Mahajan S, Morgan C, Griffiths M, Clark H, *et al*. Surfactant protein A (SP-A) inhibits agglomeration and macrophage uptake of toxic amine modified nanoparticles. *Nanotoxicology* 2015;9:952–962.
22. Schneider CA, Rasband WS, Eliceiri KW. NIH Image to ImageJ: 25 years of image analysis. *Nat Methods* 2012;9:671–675.
23. Hunt AN, Clark GT, Attard GS, Postle AD. Highly saturated endonuclear phosphatidylcholine is synthesized in situ and colocated with CDP-choline pathway enzymes. *J Biol Chem* 2001;276:8492–8499.
24. Pynn CJ, Henderson NG, Clark H, Koster G, Bernhard W, Postle AD. Specificity and rate of human and mouse liver and plasma phosphatidylcholine synthesis analyzed in vivo. *J Lipid Res* 2011;52: 399–407.
25. Zhou J, You Y, Ryan AJ, Mallampalli RK. Upregulation of surfactant synthesis triggers ABCA1-mediated basolateral phospholipid efflux. *J Lipid Res* 2004;45:1758–1767.
26. Cole LK, Vance JE, Vance DE. Phosphatidylcholine biosynthesis and lipoprotein metabolism. *Biochim Biophys Acta* 2012;1821:754–761.
27. Patel II, Steuwe C, Reichelt S, Mahajan S. Coherent anti-Stokes Raman scattering for label-free biomedical imaging. *J Opt* 2013;15:094006.

28. Gao L, Wang Z, Li F, Hammoudi AA, Thrall MJ, Cagle PT, Wong ST. Differential diagnosis of lung carcinoma with coherent anti-Stokes Raman scattering imaging. *Arch Pathol Lab Med* 2012;136: 1502–1510.
29. Le TT, Ziemba A, Urasaki Y, Brotman S, Pizzorno G. Label-free evaluation of hepatic microvesicular steatosis with multimodal coherent anti-Stokes Raman scattering microscopy. *PLoS One* 2012;7:e51092.
30. Zoumi A, Yeh A, Tromberg BJ. Imaging cells and extracellular matrix in vivo by using second-harmonic generation and two-photon excited fluorescence. *Proc Natl Acad Sci USA* 2002;99: 11014–11019.
31. Werner A, Havinga R, Bos T, Bloks VW, Kuipers F, Verkade HJ. Essential fatty acid deficiency in mice is associated with hepatic steatosis and secretion of large VLDL particles. *Am J Physiol Gastrointest Liver Physiol* 2005;288:G1150–G1158.
32. Vance DE. Role of phosphatidylcholine biosynthesis in the regulation of lipoprotein homeostasis. *Curr Opin Lipidol* 2008;19:229–234.
33. Bates SR, Tao JQ, Collins HL, Francone OL, Rothblat GH. Pulmonary abnormalities due to ABCA1 deficiency in mice. *Am J Physiol Lung Cell Mol Physiol* 2005;289:L980–L989.
34. Bates SR, Tao JQ, Yu KJ, Borok Z, Crandall ED, Collins HL, Rothblat GH. Expression and biological activity of ABCA1 in alveolar epithelial cells. *Am J Respir Cell Mol Biol* 2008;38:283–292.
35. Tsao FH, Zachman RD. Phosphatidylcholine-lysophosphatidylcholine cycle pathway enzymes in rabbit lung. I. Subcellular localization and properties. *Pediatr Res* 1977;11:849–857.
36. Caesar PA, McElroy MC, Kelly FJ, Normand IC, Postle AD. Mechanisms of phosphatidylcholine acyl remodeling by human fetal lung. *Am J Respir Cell Mol Biol* 1991;5:363–370.
37. Chen X, Hyatt BA, Mucenski ML, Mason RJ, Shannon JM. Identification and characterization of a lysophosphatidylcholine acyltransferase in alveolar type II cells. *Proc Natl Acad Sci USA* 2006;103:11724–11729.
38. Zhao GJ, Yin K, Fu YC, Tang CK. The interaction of ApoA-I and ABCA1 triggers signal transduction pathways to mediate efflux of cellular lipids. *Mol Med* 2012;18:149–158.
39. Phillips MC. Molecular mechanisms of cellular cholesterol efflux. *J Biol Chem* 2014;289:24020–24029.
40. Baldán A, Gomes AV, Ping P, Edwards PA. Loss of ABCG1 results in chronic pulmonary inflammation. *J Immunol* 2008;180:3560–3568.
41. Thomassen MJ, Barna BP, Malur AG, Bonfield TL, Farver CF, Malur A, Dalrymple H, Kavuru MS, Febbraio M. ABCG1 is deficient in alveolar macrophages of GM-CSF knockout mice and patients with pulmonary alveolar proteinosis. *J Lipid Res* 2007;48: 2762–2768.
42. Kennedy MA, Barrera GC, Nakamura K, Baldán A, Tarr P, Fishbein MC, Frank J, Francone OL, Edwards PA. ABCG1 has a critical role in mediating cholesterol efflux to HDL and preventing cellular lipid accumulation. *Cell Metab* 2005;1:121–131.
43. Côté M, Provost PR, Tremblay Y. Apolipoprotein A-I, A-II, and H mRNA and protein accumulation sites in the developing lung in late gestation. *BMC Res Notes* 2011;4:235.
44. Provost PR, Tremblay Y. Elevated expression of four apolipoprotein genes during the 32-35 week gestation window in the human developing lung. *Early Hum Dev* 2010;86:529–534.
45. Brackmann C, Gabrielsson B, Svedberg F, Holmaang A, Sandberg AS, Enejder A. Nonlinear microscopy of lipid storage and fibrosis in muscle and liver tissues of mice fed high-fat diets. *J Biomed Opt* 2010;15:066008 .
46. Romero F, Shah D, Duong M, Stafstrom W, Hoek JB, Kallen CB, Lang CH, Summer R. Chronic alcohol ingestion in rats alters lung metabolism, promotes lipid accumulation, and impairs alveolar macrophage functions. *Am J Respir Cell Mol Biol* 2014;51: 840–849.
47. Enaud L, Hadchouel A, Coulomb A, Berteloot L, Lacaille F, Boccon-Gibod L, Boulay V, Darcel F, Griese M, Linard M, *et al*. Pulmonary alveolar proteinosis in children on La Réunion Island: a new inherited disorder? *Orphanet J Rare Dis* 2014;9:85 .
48. Hu C, Wang Y, Fan Y, Li H, Wang C, Zhang J, Zhang S, Han X, Wen C. Lipidomics revealed idiopathic pulmonary fibrosis-induced hepatic lipid disorders corrected with treatment of baicalin in a murine model. *AAPS J* 2015;17:711–722.